



Waveguide-based total internal reflection fluorescence microscope enabling cellular imaging under cryogenic conditions

QINGRU LI,^{1,2,*} CHRISTIAAN N. HULLEMAN,^{1,2}  ROBERT J. MOERLAND,¹ ELIL MAILVAGANAM,¹ SRIVIDYA GANAPATHY,¹ DAAN BRINKS,¹  SJOERD STALLINGA,¹  AND BERND RIEGER¹

¹ Department of Imaging Physics, Delft University of Technology, Lorentzweg 1, 2628CJ Delft, The Netherlands

² These authors contributed equally

*q.li-9@tudelft.nl

Abstract: Total internal reflection fluorescence (TIRF) microscopy is an important imaging tool for the investigation of biological structures, especially the study on cellular events near the plasma membrane. Imaging at cryogenic temperatures not only enables observing structures in a near-native and fixed state but also suppresses irreversible photo-bleaching rates, resulting in increased photo-stability of fluorophores. Traditional TIRF microscopes produce an evanescent field based on high numerical aperture immersion objective lenses with high magnification, which results in a limited field of view and is incompatible with cryogenic conditions. Here, we present a waveguide-based TIRF microscope, which is able to generate a uniform evanescent field using high refractive index waveguides on photonic chips and to obtain cellular observation at cryogenic temperatures. Our method provides an inexpensive way to achieve total-internal-reflection fluorescence imaging under cryogenic conditions.

© 2021 Optical Society of America under the terms of the [OSA Open Access Publishing Agreement](#)

1. Introduction

1.1. TIRF microscopy

Conventional fluorescence microscopes typically excite fluorophores with freely propagating light. Total internal reflection fluorescence (TIRF) microscopy provides a way to observe and study membrane-associated processes near the plasma membrane of cells or structures' interfaces that adhere to slides, with non-propagating waves, i.e. the evanescent field [1]. When a light beam travels from a high-refractive-index material into a low-refractive-index medium, and if the incidence angle is greater than the critical angle, then total internal reflection (TIR) occurs and no light propagates into the low-refractive-index medium. An evanescent field is generated during the TIR process between these two media. Instead of freely propagating, the evanescent field is exponentially decaying, therefore, only fluorophores in a layer up to 100-200 nm from the interface are effectively excited [2]. Evanescent fields for imaging are commonly produced by high numerical aperture (NA) objective lenses in order to obtain supercritical angles and large-angle emission collection [2]. As the excitation and emission light beams are transmitted by the same objective lens, imaging results of objective-based TIRF microscopes can be influenced by the performance of the objective lens as well as by the scattered light and by auto-fluorescence. Another restriction of objective-based TIRF microscopes is the limited field of view. Though approaches have been proposed, improving the field of view up to $200 \times 200 \mu\text{m}$ [3,4], the field of view is still limited by high NA objectives for emission collection [5]. Prism-based TIRF microscopy setups can be used to generate an evanescent field and obtain imaging results with a higher signal-to-noise ratio, but the sample mounting protocols and sample movements are limited by the bulky prism components [6–8].

An alternative way to create an evanescent field can be achieved by employing planar waveguides. The concept of evanescent field generation with high-refractive-index contrast (HIC) planar waveguides was initially proposed by Lukosz and Tiefenthaler in 1983 [9] and developed as biosensors for biochemical and biological applications without [10–12] and with [13–15] labeling techniques. Since the publication by Grandin et al. more than 15 years ago [16], waveguide-based TIRF microscopy has received more attention during recent years in the field of fluorescence microscopy. Waveguides with the fabrication of ion-exchanged film [17], polymer materials [18,19], glass [20], and photonic-integrated-circuit chips [21–25] were reported for TIRF microscopy. Among them, waveguide chips can achieve imaging with large field-of-view up to millimeter scale [5,21] and can support super resolution, including single molecule localization microscopy (SMLM) [21–23], fluctuation-based super-resolution imaging [21,25], and structured illumination microscopy [24]. Although these techniques were reported to have capabilities of achieving fluorescence imaging with evanescent-field excitation, none of them have been demonstrated to be compatible with cryogenic conditions.

1.2. TIRF on a chip

Our work is based on a waveguide-based TIRF microscope which can work at both room and cryogenic temperatures. Samples are mounted on around 1-cm² chips made of HIC materials instead of glass-slides/coverlips. The chips used for the evanescent field generation are based on a Silicon (Si) substrate, with a buffer layer of Silicon Dioxide (SiO₂), followed by a thin top layer made from Silicon Nitride (Si₃N₄), as shown in Fig. 1. The Si substrate and the SiO₂ layer have thicknesses of 1 mm and 2 μm, respectively. The Si₃N₄ layer, with a thickness of about 150 nm and a width of around 40-50 μm, functions as a waveguide for the propagation of light. These three different materials have different refractive indices (*n*). After the laser beam is coupled into one end-facet of the waveguide, TIR at the low refractive-index boundaries made of SiO₂ results in an exponentially decaying evanescent wave with around 100-150 nm penetration depth just above the waveguide [22]. The evanescent field is used to illuminate specimens and in this way, only stained structures very close to the waveguide are excited and emit light. However, the waveguide allows multimode propagation, accordingly, laser beams traveling through it result in branched patterns due to scattering arising from weak inhomogeneities in e.g. waveguide thickness [26,27]. The resulting branched light patterns in the waveguide are highly dependent on the input laser beam position and polarization, as these determine the set of transmission channels that are excited [26]. The evanescent fields used for fluorescence excitation are therefore inhomogeneous. We employed a galvo mirror to quickly scan the input laser beam over the facet of the waveguide, with a scanning rate much faster than the exposure time, in order to average over the different transmission channels and achieve uniform illumination.

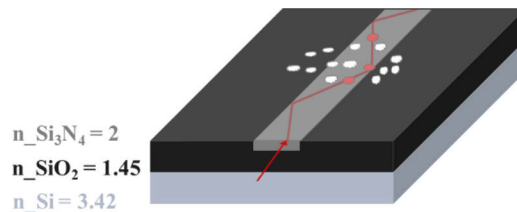


Fig. 1. The principle of evanescent field generation with a photonic-chip. The chip is made out of HIC materials with different refractive index values *n*. The high-*n* Si₃N₄ layer functions as the waveguide for light propagation. The evanescent field is created at the surface of the waveguide and used for excitation in fluorescence imaging. The white dots indicate the stained sample, and the red dots show parts of the sample that are illuminated by an idealized single ray indicated with the red line.

1.3. Imaging at cryogenic temperatures

Our setup can image samples at ambient temperatures, but also at cryogenic temperatures. Photo-bleaching is a common issue in fluorescence microscopy at room temperatures, resulting in a limited imaging time and photon yield. At cryogenic temperatures, the photo-bleaching reaction rate is reduced because of the increased photochemical stability of fluorophores [28–30]. The number of photons emitted by a single molecule determines for a large part the localization precision in SMLM [31]. The photon yield of fluorophores can be one to two orders of magnitude higher at low temperatures [30,31], and several SMLM methods have been reported to achieve sub-nanometer localization precision under cryogenic conditions [32–34]. TIRF microscopy is used in many SMLM imaging settings to reduce background influence but also for dynamic imaging, playing an important role in the study of events near cell plasma membranes. So far, TIRF microscopy is not well matched to cryogenic conditions due to the lack of high-NA cryogenic objectives. New design with high-NA super-hemispherical solid immersion lenses (*superSILs*) have been used to overcome the NA limit [35] and open up possibilities for TIRF imaging at cryogenic conditions, but this requires delicate and difficult sample preparation with the reported 1 mm diameter *superSILs* as sample holders. The waveguide-based cryogenic TIRF microscope reported in this paper may open ways to advance cellular membrane imaging.

2. Material and method

2.1. Sample preparation

Fluorophores (ATTO 647N, ATTO-TEC) were used to investigate the homogeneity of illumination generated on the waveguide as well as the fluorophore behavior at both room and cryogenic temperatures. In these two cases, the organic dye was diluted with Milli-Q water to a concentration of 10^{-6} and 10^{-7} mol/L, respectively, then spin-coated at 3000 rpm for 4 min after pipetting the solution onto cleaned chips. To assess the drift performance of the microscope, deep red fluorescent beads (PS-Speck Microscope Point Source Kit, ThermoFisher) with a diameter of 175 nm were employed. The bead solution was obtained by diluting the stock concentrations with Milli-Q water in a ratio of 1:10. In order to observe individual beads, a thin layer of sparsely distributed beads on the chip was generated after spin-coating at 3000 rpm for 4 min. For realizing cellular imaging, fixed and stained HEK293T cells were plated on waveguides. The chips were coated with fibronectin (FC010, Merck) prior to plating to facilitate cell attachment. HEK293T cells were grown on the chips to 70–80% confluence in Dulbecco's modified Eagle's medium 10 (DMEM10, Fisherscientific) at 37°C, 5% CO₂. The cells were stained with CellMask Deep Red Plasma membrane Stain (C10046, Invitrogen) for 10 minutes at 37 °C, then fixed in 4% paraformaldehyde for another 10 minutes at 37 °C. The chips were finally rinsed thrice with PBS prior to imaging.

2.2. Experimental setup

The concept of our waveguide-based cryogenic TIRF (cryo-TIRF) microscope setup is illustrated in Fig. 2. This custom-made setup employs a 658-nm red laser (LDM658.130.CWA.L, Omicron) as the source, noting that all power values mentioned in this report refer to the nominal values. The excitation beam is passed through filter 1 (ZET405/488/561/640m-TRF, Chroma), as shown in Fig. 2(a). A galvo mirror (GVS001, Thorlabs) driven by a sinusoidal signal is used to scan the input laser beam, enabling translation of the incidence position on the interface of the waveguide. The laser beam is focused onto the end-facet of the waveguide and coupled into it via a 10x/0.3 NA objective lens 1 (Plan Fluor, Nikon). As the galvo mirror requires 0.8 Volt to achieve a tilt angle of 1 degree and the width of the waveguide is around 40–50 μm, voltages of 50–100 mV are required to scan the incident light over the width of the waveguide at a scanning frequency of 100 Hz. The light propagating in the waveguide can produce an evanescent field to excite the

samples on the chip. The emission from fluorophores is collected by a 50x/0.8 NA objective lens 2 (TU Plan Fluor EPI, Nikon). Filter 2 (ET705/72 m, Chroma) suppresses the excitation laser reflection and non-fluorescent background, blocking the signal other than the desired emission signal. After being focused by a tube lens (ITL200, Thorlabs), the light signal is captured by an sCMOS camera (Zyla 4.2, Andor) with a pixel size of 6.5 μm , resulting in a back-projected pixel size of 130 nm. Two objective lenses and the chip are placed in a vacuum tank as shown in Fig. 2(b), which is pumped to a pressure of less than $5 \cdot 10^{-6}$ mbar during imaging. The chip is stuck to a copper holder with a thin layer of Apiezon N, then fits to a copper finger (with iron inlaid in the center) using a small magnet through the vacuum window, as shown in Supplement 1, Fig. S1. The copper finger is connected to the cooling tank and the sample xyz stage, enabling cooling down and three-dimension adjustment of specimens. The chip is cooled down to 97 K (-176°C) with around 3 liters of liquid nitrogen and can provide about 2.5 hours for measurement under cryogenic conditions. All recorded camera pixel values A in Analog-Digital Units (ADUs) were converted to intensities in photon count units I by calibration of the gain G and offset O_{zero} [36,37]. The intensity measured in photon counts was subsequently calculated by using the equation $I = G(A - O_{\text{zero}})$.

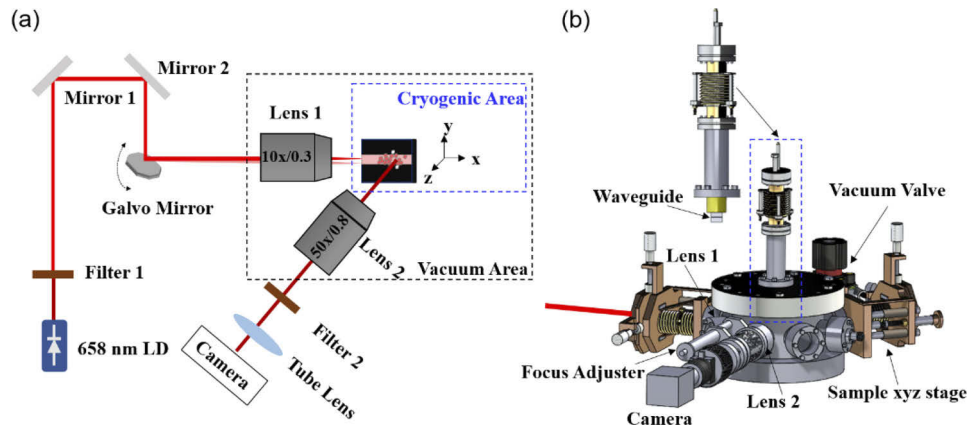


Fig. 2. Schematic diagram of our waveguide-based cryo-TIRF setup. (a) Diagram of the light path. A 658-nm laser diode provides excitation, and a galvo mirror enables input laser shift over the width of waveguides. Objective lens 1 focuses laser beams onto the end-facet of the waveguide. The emission is captured via the combination of objective lens 2 and the tube lens, and recorded by the camera. (b) Three-dimensional sketch shows optical components from Lens 1 to the camera, following the light path. Two objective lenses and the sample are placed into a vacuum tank such that the sample can be imaged at cryogenic temperatures, while the corresponding adjusters are not included in the vacuum area. The sample is cooled down using liquid nitrogen when performing imaging under cryogenic temperatures. The cryogenic area is indicated by the blue dashed box.

3. Results and discussion

3.1. Uniform illumination achieved by mode averaging

In order to create the evanescent field for uniform illumination, a galvo mirror was used in the cryo-TIRF setup to scan the laser beam at rapid speed. For better illustration of this process, ATTO 647N dye with a dense concentration of 1 μM was used to visualize the illumination patterns on waveguides at room temperatures. Figure 3 shows camera images of spin-coated ATTO 647N dye for different scanning rates of the input laser beam. The nominal power of the input laser was set to be 10 mW, to avoid severe photo-bleaching. The camera exposure time was

0.1 s with a framerate of 10 frames-per-second (fps) during imaging acquisition, and 100 frames were captured. When the incident laser was scanned at a low frequency of 100 mHz (Fig. 3(a) and Visualization 1), we observed random branched patterns of light, changing with the excitation during the scanning procedure. This wave phenomenon is known as branched flow, and results from weak scattering by e.g. non-uniformities in the waveguide thickness or slightly diffuse or non-sharp edges of the waveguide [26,27]. Based on the 100 frames with branched multimode patterns, we calculated the normalized autocorrelation function $\langle C(x') = I(x)I(x - x') \rangle / \langle I \rangle^2$ along the direction parallel to the waveguide, and subsequently averaged the normalized autocorrelation over each horizontal position and frame. The averaged autocorrelation function $C(x')$ shown in Fig. 3(b) is fitted well with an exponentially decaying function, in agreement with expectations. The fit points to a correlation length $\xi = 19 \mu\text{m}$, which thus characterizes the length scale of non-uniformity of the waveguide. The spatially correlated non-uniform illumination patterns may have an impact on the reconstruction results of fluctuation-based super-resolution imaging methods [25].

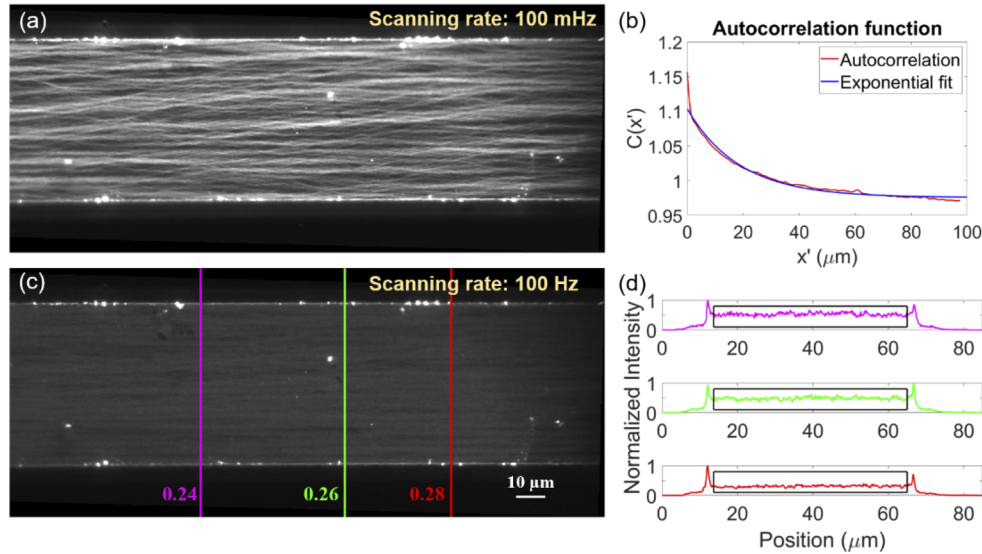


Fig. 3. Camera images of (averaged) illumination patterns for excitation with different scanning rates. (a) Illumination pattern with a low scanning frequency of 100 mHz. (b) Normalized autocorrelation plot and the corresponding exponential fit of the multimode patterns shown in (a) and Visualization 1. (c) Mode-averaged uniform illumination pattern resulting from 100 Hz scanning speed. The values (0.24, 0.26, and 0.28) beside the vertical lines indicate modulation depths along the corresponding profile lines. (d) The normalized intensities of captured values along three profile lines, with corresponding colors indicated in (c). Measured values outside the waveguide and near boundaries were ignored when calculating the modulation depth.

Homogeneity of illumination for SMLM is significant, as un-uniform illumination causes un-even switching rates, resulting low imaging quality. For our experiments, uniform illumination is desirable and was obtained with high-frequency scanning input laser. When the scanning frequency was increased to 100 Hz, 10 full-waveguide scans were achieved in one camera exposure. The resulting averaged light field in the waveguide becomes more uniform as shown in Fig. 3(c) and Visualization 2 as a result of mode averaging. The boundaries of the waveguide are visible in both Fig. 3(a) and (c) where the dark part is outside the waveguide. Regions with high brightness come from a more dense fluorophore distribution, which may be a result of

imperfect procedures during chip cleaning and/or sample spin-coating. In order to evaluate the homogeneity of the more uniform excitation obtained with a higher scanning rate of 100 Hz, we evaluated the modulation depth, also known as modulation index. We computed the modulation depth from $(A_{max} - A_{min}) / (A_{max} + A_{min})$, where A_{max} and A_{min} are the maximum and minimum amplitudes of the signal. Modulation depth with a smaller value means less intensity variation, indicating a more uniform light field distribution. Several values of modulation depths were calculated along different profile lines, indicated with different colors in Fig. 3(c). The corresponding line profiles are shown in Fig. 3(d). The edge artifacts were neglected and only data enclosed in black boxes were used when calculating the values of modulation depth. We find values 0.24 ± 0.05 , 0.26 ± 0.05 , and 0.28 ± 0.03 for the three line profiles. These values are comparable to the reported modulation depth value of 0.25 from Ref. [22].

Further improvements on generating uniform illumination could be achieved by using an incoherent light source. LEDs with low temporal and spatial coherence could be used to enhance the homogeneity of evanescent field, but the coupling of light into a narrow waveguide with a width of $\sim 50 \mu\text{m}$ and a thickness of $\sim 150 \text{ nm}$ may be ineffective. Superluminescent diodes with wide spectrum could replace the laser diode in our setup, expecting to achieve more uniform illumination field by mode averaging. Combining the existed laser diode with a rotating diffuser can also be helpful in reducing laser coherence, but fiber optics are required for avoiding scattering problem. Moving parts and additional optics can decrease the stability and sensitivity of the system.

3.2. Investigation of fluorophore behavior under cryogenic conditions

The images shown in Fig. 3 were acquired under room temperature conditions in a vacuum, such that we could exclude potential thermal drift of the setup under cryogenic conditions. For our cryo-TIRF microscope, the main focus is the improvement of fluorophore behavior at cryogenic temperatures. We used spin-coated ATTO 647N with a concentration of $0.1 \mu\text{M}$ to study the fluorophore behavior at both room and cryogenic temperatures. In both cases, the input laser power was 130 mW and the scanning rate was 100 Hz. At room temperatures, 1535 in-focus frames were captured with 0.2 s exposure time at 1 fps. The first 60 frames were discarded to get rid of the disturbance from the operator and/or setup instability when starting the measurement. The time-course of the normalized fluorescence intensity is shown in Fig. 4(a). After measurement with high excitation power at room temperatures, the same sample was cooled to 97 K. The cooling procedure for our cryostat takes about 1.5 hours, offering about 2.5 hours for imaging at cryogenic conditions. At cryogenic temperatures, the sample went out-of-focus after several minutes due to drift, therefore we monitored the signal and manually refocused during the data acquisition. The camera exposure time was increased to 0.8 s for an increase of measured values A in ADU, since a significant part of the fluorescent molecules were bleached after imaging at room temperatures. In total 1490 frames at 1 fps were used to estimate photon counts. The normalized fluorescence intensity shown in Fig. 4(b) displays the result of photon counting under cryogenic temperatures.

The corresponding fitted photo-bleaching curves of the different temperatures are also shown in Fig. 4. The photon count of ATTO 647N decays bi-exponentially indicating that there are two different pathways of photo-bleaching [38]. A single exponential fit did not represent the acquired data well. According to the bi-exponential fit, at room temperatures, the main bleaching time is $2.5 \cdot 10^3 \text{ s}$, with a precision of fit obtained from computing the estimated variance-covariance matrix of the fitted coefficients of 0.3%. At cryogenic temperatures, the bleaching time is $1.4 \cdot 10^4 \text{ s}$, with a precision of fit of 2%, about 5.5 times longer than that at room temperatures. The recorded data at cryogenic temperatures show more fluctuation around the mean decay curve compared to the room temperatures curve. The root mean square error (RMSE) between the data and the fit is calculated to be 0.014. There are several possible reasons for this, one may be

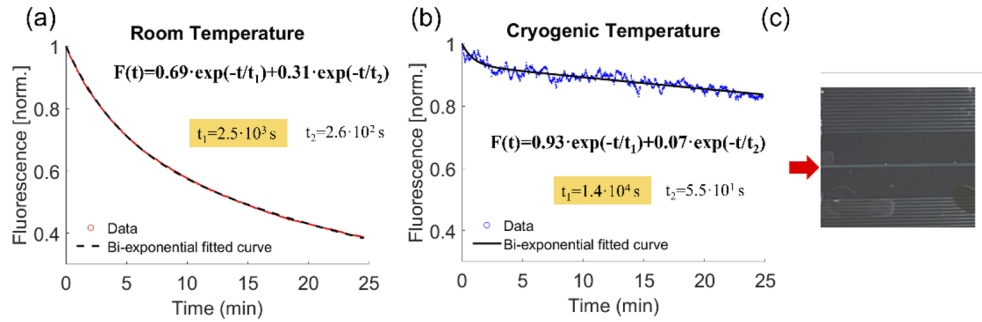


Fig. 4. Photo-bleaching curves of ATTO 647N at room (a) and cryogenic temperatures (b). Photon counts decay bi-exponentially. The fitted curves are indicated by $F(t)$. The highlighted t_1 values represent the bleaching times obtained from the fits. (c) The waveguide in grey centrally located on the square chip was coupled with input laser (presented by red big arrow) in both cases.

the manual focus adjustments during experiments, another could come from drift of the setup. The temperature difference between the inside and outside of the cryostat is large (~ 200 K), the heat leaks from the outside towards the cold cryostat are significant when imaging at cryogenic conditions. The interaction between the cryostat towards the sample holder and ambient air could cause these disturbances. As both objective lenses are placed inside the vacuum tank but outside the cryogenic area, they are also subject to thermal gradients and thus influence the stability of the acquisition. The movement of objective lens 1 has an impact on the in-coupling efficiency of the laser beam, leading to varying excitation intensity during the measurement. The drift of objective lens 2 can cause focus problems during imaging and introduce defocus.

We have studied the effect of in-coupling on the image at cryogenic temperatures, by pointing the laser over the surface of the waveguide instead of coupling the laser into the waveguide. The sample imaged in this way had the same concentration and preparation procedures as before. This kind of excitation could reduce the impact of laser-coupling on the observed drift as the light is not focused. In this way, it could help us figure out the cause of the random signal oscillation shown in Fig. 4(b). The excitation power density was much smaller compared to the last experiment because of the unfocused incident beam, although the average power was set to be the same (130 mW). In Fig. 5 we show photo-bleaching curves for ~ 3000 frames, which were captured during 50 minutes under both room and cryogenic imaging conditions. At room temperatures, the bleaching time is about $1.7 \cdot 10^4$ s with fit precision of 0.3%, according to the fitted curve shown in Fig. 5(a), where the longer bleaching time may be caused by the unfocused excitation. The room-temperature data show a larger fluctuation level compared to Fig. 4(a), which may come from the non-uniform distribution of ATTO 647N dye and/or the shift of the excitation laser beam during the measurement. At cryogenic temperatures, the bleaching time is around $1.1 \cdot 10^5$ s, with fit precision of 0.9%, which is about 6 times longer for the same ATTO 647N sample imaging at room temperatures. The signal variations around the mean decay curve here are modest compared to Fig. 4(b), which is also reflected in a better precision of fit. The RMSE value between the data and the fit is about 0.004, indicating a smoother intensity decay. The small jumps shown in Fig. 5(b) may result from the manual focus adjustments during data acquisition. For all data (measured with evanescent field or non-evanescent field), the in-coupling problem to the waveguides is demonstrated to be significant, especially when imaging under cryogenic temperatures. We suspect that the drift of the system is the main reason for the in-coupling issue.

The drift of the setup influences the image quality and maximum imaging time. In order to study the drift of our setup, 175-nm fluorescent beads were spin-coated on the chip and

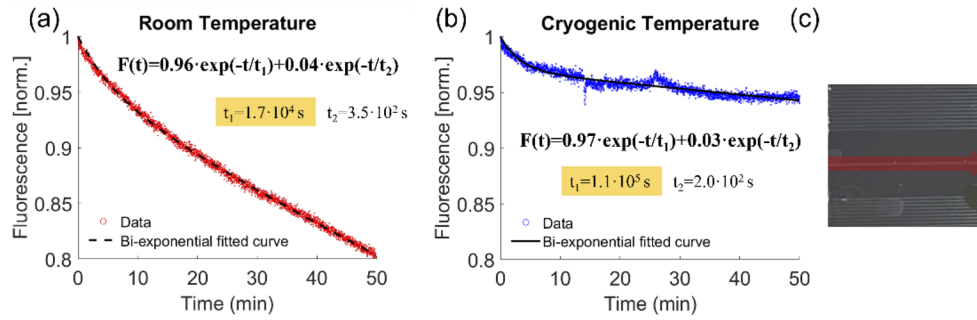


Fig. 5. Photo-bleaching curves of ATTO 647N excited by non-evanescent fields at room (a) and cryogenic temperatures (b). Photon counts decrease bi-exponentially as shown in Fig. 4. The fitted curves are indicated by $F(t)$. The highlighted t_1 values indicate the bleaching times obtained from the fits. (c) The red big arrow indicates that the laser beam used for excitation went across the chip surface, instead of being in-coupled into the waveguide.

imaged at both room and cryogenic temperatures. During the measurement, the input laser had a nominal power of 10 mW and the acquisition rate was 1 fps. The incident laser was not focused and coupled into waveguides, but aimed over the chip to illuminate the beads spin-coated on the imaging plane to decrease the influence of in-coupling. The localization and tracking of individual beads were done using ThunderSTORM [39] based on Fiji software [40]. Figure 6 shows the displacements of the image plane, in directions parallel (x) and perpendicular (y) to the waveguide. The displacement along the axial direction can be inferred from the in-focus time during acquisition, but it is hard to quantify this precisely from the current experiments. We observe that the drift along the y direction is larger than along the x direction (compare Fig. 6(a) and (b)). In-focus frames used for localization and tracking can be captured after being exposed for about 50 minutes. Compared with ATTO 647N dye, the acquisition time of in-focus frames is much longer, which may result from the stronger brightness and sparser distribution of the bead sample as shown in Fig. 6(c). At cryogenic temperatures, the acquisition time was much shorter as shown in Fig. 6(d) and (e), which indicates that the displacement along the axial direction of the sample (shown by Fig. 6(f)) was larger. The same holds for the displacements along the x and y directions. When imaging at cryogenic conditions, the drift of the setup increased significantly and results in shortened measurement time. For fixed cellular imaging, the performance of this setup seems sufficient. In our setup, thermal drift appears a major issue when imaging at cryogenic conditions, because of the common issue of heat conduction between the low-temperature inside and room-temperature outside the cryostat. Metal parts of the cryostat and the parts of objective lenses outside the cryostat are considered as the main channels for heat conduction between the cryostat and the ambient air. We employed polyether ether ketone spacers between the sample holder finger and metal parts for heat isolation. The thermal drift problem could be further diminished by including the two objective lenses in the cryogenic zone and installing electrically controlled feedback stages. The out-of-focus problem can also be solved by introducing auto-focus via a feedback system.

3.3. Imaging the plasma membrane of HEK293T cells

We achieved successful observation of biological structures with this waveguide-based cryo-TIRF microscope. Figure 7 shows HEK293T cells stained with plasma membrane dye. The HEK293T cells were plated on the chip, and the two red lines in each subfigure indicate the boundaries of the waveguide. We used two kinds of illumination, using the evanescent field generated on the waveguide and using the non-evanescent field produced by an unfocused laser beam propagating

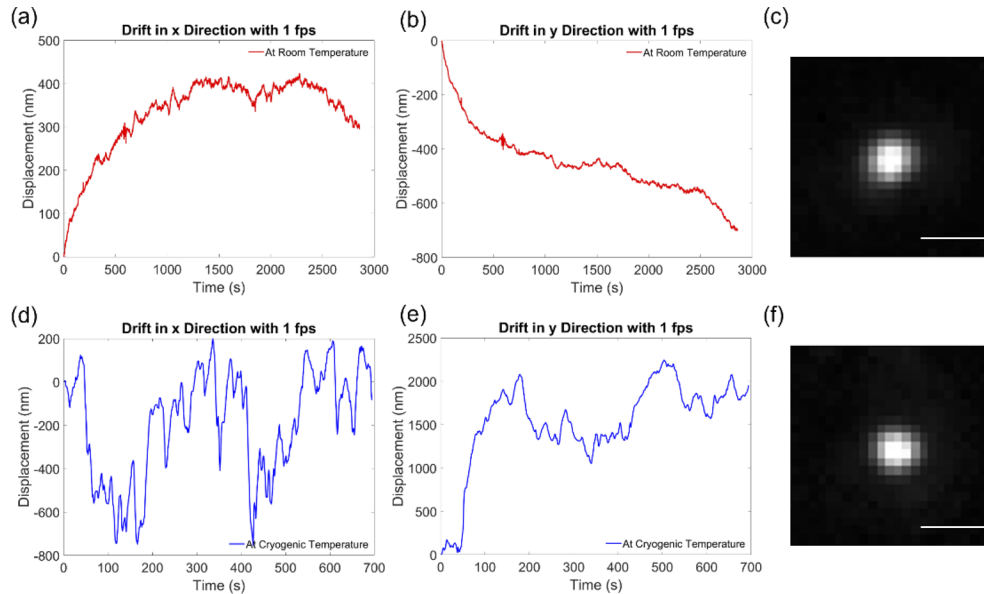


Fig. 6. Drift measurements with fluorescent bead samples. Displacements along horizontal (x) and vertical (y) direction with increasing time, at room temperatures (in red) and cryogenic conditions (in blue). (c, f) Images of the fluorescent beads. Scale bars, 1 μm.

on the chip surface. The imaging results under TIRF and non-TIRF conditions were recorded at both room and cryogenic temperatures. Specifically, the evanescent field was produced with a focused input laser with 110 mW of power at room temperatures and 60 mW at cryogenic temperatures, and the scanning frequencies of the input laser are 100 Hz in both cases for uniform illumination. Different laser powers were used to avoid saturated fluorescence intensity during data acquisition. When HEK293T cells were illuminated by the evanescent field, cell membranes that attached to the waveguide can be visualized as shown in Fig. 7(a) and (b), while structures beyond the boundaries can be hardly observed. When the same region of HEK293T cells was excited by non-evanescent fields with a laser power of 1 mW, the membrane outside the waveguide shown in Fig. 7(c) and (d) can be visualized as well. At room and cryogenic temperatures, the imaging results of the same sample did not show much difference in terms of structural information, although the image contrasts were observed to be different. This may result from the larger drift at cryogenic conditions, as discussed in the last section. Another drawback of our design is the low collection efficiency of the emission from high-n waveguides, compared with traditional TIRF microscope where the emission is collected from evanescent field side with a high-NA objective. We estimated the collection efficiency of our waveguide-based TIRF imaging with a theoretical model [41,42], and found the percentages of emission of fluorescence contacted to waveguide surface collected by the objective lens to be ~3.92% and ~0.64% for dipoles parallel and normal to the surface, respectively. Compared with the objective-based TIRF imaging method, which has a collection efficiency of around 10%-20% [43], waveguide-based TIRF microscopy performs worse in emission detection because most part of emission intensity is coupled back to the high-n waveguide instead of being released in a vacuum and collected by a respectively low NA objective lens.

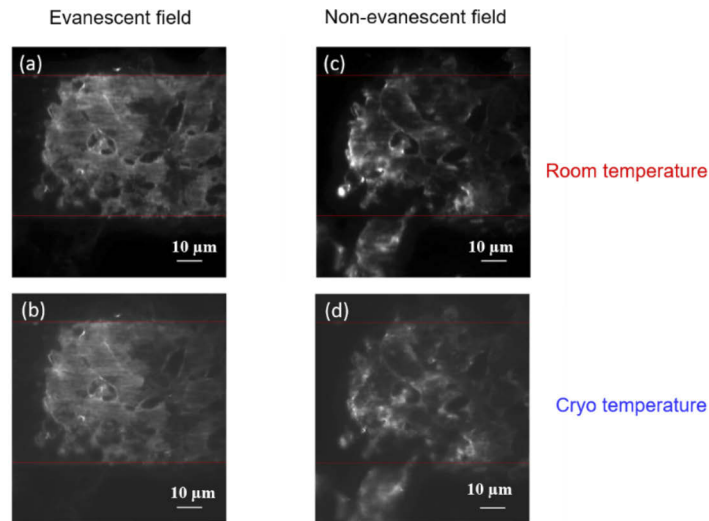


Fig. 7. Imaging results of fixed HEK293T cells, which were stained with red plasma membrane dye. Panels (a) and (b) show the membranes near the interface of waveguide excited by evanescent fields at room and cryogenic temperatures, respectively. Panels (c) and (d) show HEK cell membrane images under non-TIRF imaging conditions.

4. Conclusion

In this paper, we report a waveguide-based TIRF microscope capable of cellular imaging at cryogenic conditions, showing an increased photo-stability of fluorophores. Evanescent fields produced over waveguides were used for excitation, and uniform illumination was achieved using mode averaging by high-frequency scanning of the excitation laser beam coupled into the waveguide. Photo-bleaching under cryogenic conditions was studied using ATTO 647N, indicating a five to six-fold increase in bleaching time. Drift was investigated in our setup with fluorescent beads samples, showing a two to three-fold increase compared to room temperature conditions. We showed that our cryo-TIRF microscope is capable of imaging fixed cellular samples, enabling observations of the plasma membrane.

Funding. Nederlandse Organisatie voor Wetenschappelijk Onderzoek (VICI grant no. 17046).

Acknowledgments. We thank Balpreet S. Ahluwalia, Øystein I. Helle, and Jean-Claude Tinguely for the chips. This work was supported by the Dutch Research Council (NWO), VICI grant no. 17046 for B.R. and Q.L.

Disclosures. The authors declare no conflicts of interest.

Data availability. Data underlying the results presented in this paper are not publicly available at this time. These data may be obtained from the authors upon reasonable request.

Supplemental document. See [Supplement 1](#) for supporting content.

References

1. D. Axelrod, "Cell-substrate contacts illuminated by total internal reflection fluorescence," *J. Cell Biol.* **89**(1), 141–145 (1981).
2. A. L. Mattheyses and D. Axelrod, "Direct measurement of the evanescent field profile produced by objective-based total internal reflection fluorescence," *J. Biomed. Opt.* **11**(1), 014006 (2006).
3. M. Cardoso Dos Santos, R. Déturche, C. Vézy, and R. Jaffiol, "Topography of cells revealed by variable-angle total internal reflection fluorescence microscopy," *Biophys. J.* **111**(6), 1316–1327 (2016).
4. A. Mau, K. Friedl, C. Leterrier, N. Bourg, and S. Lévêque-Fort, "Fast widefield scan provides tunable and uniform illumination optimizing super-resolution microscopy on large fields," *Nat. Commun.* **12**(1), 1–11 (2021).

5. A. Ahmad, V. Dubey, N. Jayakumar, A. Habib, A. Butola, M. Nystad, G. Acharya, P. Basnet, D. S. Mehta, and B. S. Ahluwalia, "High-throughput spatial sensitive quantitative phase microscopy using low spatial and high temporal coherent illumination," *Sci. Rep.* **11**(1), 1–13 (2021).
6. D. Axelrod, N. L. Thompson, and T. P. Burghardt, "Total internal reflection fluorescent microscopy," *J. Microsc.* **129**(1), 19–28 (1983).
7. D. Axelrod, T. P. Burghardt, and N. L. Thompson, "Total internal reflection fluorescence," *Annu. Rev. Biophys. Bioeng.* **13**(1), 247–268 (1984).
8. T. P. Burghardt, A. D. Hipp, and K. Ajtai, "Around-the-objective total internal reflection fluorescence microscopy," *Appl. Opt.* **48**(32), 6120–6131 (2009).
9. W. Lukosz and K. Tiefenthaler, "Directional switching in planar waveguides effected by adsorption-desorption processes," in *Technical Digest, Second European Conference on Integrated Optics, Florence, 1983, Conf. Publ. 227* (IEE, London, 1983), pp. 152–155.
10. K. Tiefenthaler, "Grating couplers as label-free biochemical waveguide sensors," *Biosens. Bioelectron.* **8**(7-8), xxxv–xxxvii (1993).
11. W. Lukosz, "Integrated optical chemical and direct biochemical sensors," *Sens. Actuators, B* **29**(1-3), 37–50 (1995).
12. R. L. Rich and D. G. Myszka, "Survey of the year 2003 commercial optical biosensor literature," *J. Mol. Recognit.* **18**(1), 1–39 (2005).
13. G. L. Duveneck, M. Pawlak, D. Neuschäfer, E. Bär, W. Budach, U. Pieleles, and M. Ehrat, "Novel bioaffinity sensors for trace analysis based on luminescence excitation by planar waveguides," *Sens. Actuators, B* **38**(1-3), 88–95 (1997).
14. A. Brecht, A. Klotz, C. Barzen, G. Gauglitz, R. D. Harris, G. R. Quigley, J. S. Wilkinson, P. Sztajnbock, R. Abuknesha, J. Gascón, A. Oubiña, and D. Barceló, "Optical immunoprobe development for multiresidue monitoring in water," *Anal. Chim. Acta* **362**(1), 69–79 (1998).
15. G. L. Duveneck, A. P. Abel, M. A. Bopp, G. M. Kresbach, and M. Ehrat, "Planar waveguides for ultra-high sensitivity of the analysis of nucleic acids," *Anal. Chim. Acta* **469**(1), 49–61 (2002).
16. H. M. Grandin, B. Städler, M. Textor, and J. Vörös, "Waveguide excitation fluorescence microscopy: A new tool for sensing and imaging the biointerface," *Biosens. Bioelectron.* **21**(8), 1476–1482 (2006).
17. A. Hassanzadeh, M. Nitsche, S. Mittler, S. Armstrong, J. Dixon, and U. Langbein, "Waveguide evanescent field fluorescence microscopy: Thin film fluorescence intensities and its application in cell biology," *Appl. Phys. Lett.* **92**(23), 233503–233504 (2008).
18. B. Agnarsson, S. Ingthorsson, T. Gudjonsson, and K. Leosson, "Evanescent-wave fluorescence microscopy using symmetric planar waveguides," *Opt. Express* **17**(7), 5075–5082 (2009).
19. B. Agnarsson, A. B. Jonsdottir, N. B. Arnfinnsdottir, and K. Leosson, "On-chip modulation of evanescent illumination and live-cell imaging with polymer waveguides," *Opt. Express* **19**(23), 22929–22935 (2011).
20. S. Ramachandran, D. A. Cohen, A. P. Quist, and R. Lal, "High performance, LED powered, waveguide based total internal reflection microscopy," *Sci. Rep.* **3**(1), 2133 (2013).
21. R. Diekmann, Ø. I. Helle, C. I. Øie, P. McCourt, T. R. Huser, M. Schüttelpeiz, and B. S. Ahluwalia, "Chip-based wide field-of-view nanoscopy," *Nat. Photonics* **11**(5), 322–328 (2017).
22. Ø. I. Helle, D. A. Coucheron, J.-C. Tinguely, C. I. Øie, and B. S. Ahluwalia, "Nanoscopy on-a-chip: super-resolution imaging on the millimeter scale," *Opt. Express* **27**(5), 6700–6710 (2019).
23. A. Archetti, E. Glushkov, C. Sieben, A. Stroganov, A. Radenovic, and S. Manley, "Waveguide-PAINT offers an open platform for large field-of-view super-resolution imaging," *Nat. Commun.* **10**(1), 1267 (2019).
24. Ø. I. Helle, F. T. Dullo, M. Lahrberg, J. C. Tinguely, O. G. Hellesø, and B. S. Ahluwalia, "Structured illumination microscopy using a photonic chip," *Nat. Photonics* **14**(7), 431–438 (2020).
25. N. Jayakumar, Ø. I. Helle, K. Agarwal, and B. S. Ahluwalia, "On-chip TIRF nanoscopy by applying Haar wavelet kernel analysis on intensity fluctuations induced by chip illumination," *Opt. Express* **28**(24), 35454–35468 (2020).
26. A. Brandstötter, A. Girschik, P. Ambichl, and S. Rotter, "Shaping the branched flow of light through disordered media," *Proc. Natl. Acad. Sci.* **116**(27), 13260–13265 (2019).
27. A. Patsyk, U. Sivan, M. Segev, and M. A. Bandres, "Observation of branched flow of light," *Nature* **583**(7814), 60–65 (2020).
28. W. E. Moerner and M. Orrit, "Illuminating single molecules in condensed matter," *Science* **283**(5408), 1670–1676 (1999).
29. C. L. Schwartz, V. I. Sarbash, F. I. Ataullakhanov, J. R. McIntosh, and D. Nicastro, "Cryo-fluorescence microscopy facilitates correlations between light and cryo-electron microscopy and reduces the rate of photobleaching," *J. Microsc.* **227**(2), 98–109 (2007).
30. R. Zondervan, F. Kulzer, M. A. Kol'chenko, and M. Orrit, "Photobleaching of rhodamine 6G in poly(vinyl alcohol) at the ensemble and single-molecule levels," *J. Phys. Chem. A* **108**(10), 1657–1665 (2004).
31. C. N. Hulleman, W. Li, I. Gregor, B. Rieger, and J. Enderlein, "Photon yield enhancement of red fluorophores at cryogenic temperatures," *ChemPhysChem* **19**(14), 1774–1780 (2018).
32. S. Weisenburger, B. Jing, A. Renn, and V. Sandoghdar, "Cryogenic localization of single molecules with angstrom precision," *Proc. SPIE* **8815**, 88150D (2013).
33. S. Weisenburger, D. Boening, B. Schomburg, K. Giller, S. Becker, C. Griesinger, and V. Sandoghdar, "Cryogenic optical localization provides 3D protein structure data with Angstrom resolution," *Nat. Methods* **14**(2), 141–144 (2017).

34. T. Furubayashi, K. Motohashi, K. Wakao, T. Matsuda, I. Kii, T. Hosoya, N. Hayashi, M. Sadaie, F. Ishikawa, M. Matsushita, and S. Fujiyoshi, "Three-dimensional localization of an individual fluorescent molecule with angstrom precision," *J. Am. Chem. Soc.* **139**(26), 8990–8994 (2017).
35. L. Wang, B. Bateman, L. C. Zanetti-Domingues, A. N. Moores, S. Astbury, C. Spindloe, M. C. Darrow, M. Romano, S. R. Needham, K. Beis, D. J. Rolfe, D. T. Clarke, and M. L. Martin-Fernandez, "Solid immersion microscopy images cells under cryogenic conditions with 12 nm resolution," *Commun. Biol.* **2**(1), 74 (2019).
36. R. Heintzmann, P. K. Relich, R. P. J. Nieuwenhuizen, K. A. Lidke, and B. Rieger, "Calibrating photon counts from a single image," <https://arxiv.org/abs/1611.05654>.
37. L. J. van Vliet, D. Sudar, and I. T. Young, "Digital fluorescence imaging using cooled CCD array cameras invisible," *Cell Biol.* **3**, 109–120 (1998).
38. T. Cordes, A. Maiser, C. Steinhauer, L. Schermelleh, and P. Tinnefeld, "Mechanisms and advancement of antifading agents for fluorescence microscopy and single-molecule spectroscopy," *Phys. Chem. Chem. Phys.* **13**(14), 6699–6709 (2011).
39. M. Ovesný, P. Křížek, J. Borkovec, Z. Švindrych, and G. M. Hagen, "ThunderSTORM: a comprehensive ImageJ plug-in for PALM and STORM data analysis and super-resolution imaging," *Bioinformatics* **30**(16), 2389–2390 (2014).
40. J. Schindelin, I. Arganda-Carreras, E. Frise, V. Kaynig, M. Longair, T. Pietzsch, S. Preibisch, C. Rueden, S. Saalfeld, B. Schmid, J.-Y. Tinevez, D. J. White, V. Hartenstein, K. Eliceiri, P. Tomancak, and A. Cardona, "Fiji: an open-source platform for biological-image analysis," *Nat. Methods* **9**(7), 676–682 (2012).
41. W. L. Barnes, "Fluorescence near interfaces: The role of photonic mode density," *J. Mod. Opt.* **45**(4), 661–699 (1998).
42. L. Novotny and B. Hecht, *Principles of Nano-Optics* (Cambridge University press, 2012), Chap. 10.
43. M. Leutenegger and T. Lasser, "Detection efficiency in total internal reflection fluorescence microscopy," *Opt. Express* **16**(12), 8519–8531 (2008).